Available online at www.sciencedirect.com
ScienceDirect
Trans. Nonferrous Met. Soc. China 34(2024) 3521−3535
Transactions of Nonferrous Metals Society of China
www.tnmsc.cn

Effect of Ni on microstructure and mechanical properties of Al−Mg−Si alloy for laser powder bed fusion

Yi-mou LUO[1], Jian-ying WANG[1], Tao WEN[1], Fei-peng YANG[1], Meng-zhen ZHU[1], Na HE[1], Jian-ming ZHENG[2], Ling SHAN[2], Hai-lin YANG[1]

1. State Key Laboratory of Powder Metallurgy, Central South University, Changsha 410083, China;
2. Zhejiang Wanfeng Precision Casting Co., Ltd., Shaoxing 312400, China

Received 4 June 2024; accepted 21 September 2024

Abstract: The microstructures and mechanical properties were systematically studied for the high-strength Al−5Mg_2Si−1.5Ni alloy fabricated by laser powder bed fusion (L-PBF). It is found that the introduction of Ni (1.5 wt.%) into an Al−5Mg_2Si alloy can significantly improve the L-PBF processibility and provide remarkable improvement in mechanical properties. The solidification range of just 85.5 K and the typical Al−Al_3Ni eutectics could be obtained in the Ni-modified Al−5Mg_2Si samples with a high relative density of 99.8% at the volumetric energy density of 107.4 J/mm^3. Additionally, the refined hierarchical microstructure was mainly characterized by heterogeneous α-Al matrix grains (14.6 μm) that contain the interaction between dislocations and Al−Al_3Ni eutectics as well as Mg_2Si particles. Through synergetic effects of grain refinement, dislocation strengthening and precipitation strengthening induced by Ni addition, the L-PBFed Al−5Mg_2Si−1.5Ni alloy achieved superior mechanical properties, which included the yield strength of (425±15) MPa, the ultimate tensile strength of (541±11) MPa and the elongation of (6.2±0.2)%.

Key words: laser powder bed fusion; Al−Mg−Si alloy; microstructural evolution; mechanical properties; strengthening mechanism

1 Introduction

In additive manufacturing (AM), laser powder bed fusion (L-PBF) has been proven to be one of the most promising technologies that can deliver great convenience in manufacturing complex structural components [1−3]. L-PBF uses a focused laser beam to selectively melt the metallic powder of raw material of complex components layer-by-layer [4,5]. Therefore, L-PBF process is characterized by the rapid solidification with high cooling rates (v: 10^5−10^6 K/s) and large temperature gradients (>10^5 K/m) in the melt pool zones, which promotes the formation of a high non-equilibrium microstructure with fine grain size. As a result, the mechanical performances tend to be improved significantly in comparison with the counterpart made by conventional processing methods [6−9].

Aluminium (Al) alloys have been widespread used in various industrial sectors owing to their high specific strength, low production cost and low density [10,11]. Currently, L-PBF is extensively developing capability in processing Al alloys and Al matrix composites to improve the mechanical properties [12,13] because their hot tearing and easy oxidation are limiting the application of L-PBF [14]. The significant challenges in L-PBFed conventional high-strength wrought Al alloys, such as Al−Cu, Al−Mg and Al−Mg−Si alloys, are the

Corresponding author: Hai-lin YANG, Tel: +86-13973182703, E-mail: y-hailin@csu.edu.cn
DOI: 10.1016/S1003-6326(24)66623-9

formation of severe hot cracks. These are always highly associated with the metallurgical force (e.g., the large solidification range and the coarse columnar grains in the microstructures [15−17]) and the mechanical force (e.g., the high residual stress induced by the extreme solidification conditions during L-PBF [18]). It is generally believed that the increased volume fraction of eutectics in L-PBFed Al alloys is an effective way to eliminate hot cracks [19−25]. On top of the widely-studied Al−Si alloys [19−22], the newly-explored near-eutectic Al−Fe [23], Al−Ce [24] and Al−Ni [25] alloys showed excellent printability in L-PBF because of the narrow solidification range and low hot crack tendency.

It is noted that the Al−Mg−Si alloys can be described as Al−Mg_2Si pseudo-binary eutectic alloy when the mass ratio of Mg to Si is 1.73. It can also be regarded as Al−Mg_2Si−Si or Al−Mg_2Si−Mg pseudo-eutectic alloys when the mass ratio of Mg to Si is not 1.73. Our previous works have demonstrated that the increased Mg_2Si content can improve the laser absorption rate and the melt fluidity of L-PBFed Al−Mg−Si alloys [6,26−29]. And the formation of fine cellular structures that are composed of α-Al phase and eutectic Mg_2Si networks shows a positive effect on inhibiting the initiation and propagation of cracks. Consequently, the mechanical properties are significantly enhanced under L-PBFed and as-aged conditions [30]. However, the understanding for L-PBFed Al−Mg_2Si alloys is limited as it is still unknown for the solidification behavior and microstructural evolution, especially for the cellular structures after introducing other eutectic elements for Al alloys, and the technical approaches to fabricate cost-effective L-PBFed Al−Mg−Si alloys with a superior combination of strength and ductility.

Nickel (Ni) is one of the popular and low-cost eutectic elements in Al alloys. Al alloys with Ni addition related to a high thermal stability of precipitates are always associated with specific mechanical performance at room and elevated temperatures [31,32]. Therefore, it is expected that the addition of Ni to the Al−5Mg_2Si alloy can further improve the formability of the alloy via the eutectic filling of Al_3Ni during the terminal stage of solidification and the in-situ high-density precipitates can contribute to the strength enhancement of the alloy through precipitation strengthening. To this end, we used an Al−5Mg_2Si−1.5Ni alloy to understand the microstructures and mechanical properties under the L-PBFed condition. The solidification sequence and microstructural evolution during L-PBF process were investigated systematically. The discussion focused on the strengthening mechanisms of the L-PBFed Al−5Mg_2Si−1.5Ni alloy. This work suggests that the introduction of Al−Al_3Ni eutectics induced via Ni addition offers an innovative design for the high-strength Al−Mg−Si alloy capable of processing for additive manufacturing.

2 Experimental

2.1 Raw materials and sample fabrication

Gas atomization was used to prepare the pre-alloyed Al−5Mg_2Si−1.5Ni alloy powder in this work. A high purity argon atmosphere (99.9%) was used to protect powders from oxidation during atomization. The detailed chemical compositions of the alloy powder and the L-PBFed sample determined by inductively coupled plasma atomic emission spectrometry (ICAP 7000 Series) are shown in Table 1. A small amount of Mg loss occurred during the L-PBF process due to the evaporation and oxidation of Mg [33]. The morphology, size and elemental distribution of the atomized Al−5Mg_2Si−1.5Ni alloy powders are displayed in Figs. 1(a−c). The pre-alloyed powder is featured by spheroidal morphology with tiny satellite particles. The volume-weighted percentiles of the Al−5Mg_2Si−1.5Ni alloy powders detected by laser particle size analyzer (Matersizer) were D_{10}=9.23 μm, D_{50}=25.1 μm, and D_{90}=60.0 μm. Meanwhile, elemental mappings in Figs. 1(b_1−b_4) confirm that Al, Mg, Si and Ni elements are homogeneously distributed in the pre-alloyed particles.

Table 1 Chemical compositions of Al−Mg−Si−Ni alloy powder and L-PBFed Al−Mg−Si−Ni alloy obtained by inductively coupled plasma atomic emission spectrometry (wt.%)

Sample	Mg	Si	Ni	Fe	Mn	Al
Al−Mg−Si−Ni powder	5.10	2.10	1.55	0.86	0.51	Bal.
L-PBFed Al−Mg−Si−Ni alloy	4.85	2.05	1.53	0.88	0.52	Bal.

L-PBF process was performed on an EP-M150 system (Eplus3D, China) equipped with a 500 W fibre laser at a laser beam size of 70 μm. The processing parameters were adopted as follows: laser powers of 270, 290, 310, 330, and 350 W, scanning speeds of 700, 900, 1100, and 1300 mm/s, a hatch spacing of 0.10 mm, and a layer thickness of 0.03 mm. L-PBFed samples were fabricated layer-by-layer on a grit-blasted AA6061 alloy plate. To avoid oxidation during L-PBF, high-purity argon was filled into a printing chamber. A schematic diagram of scanning track is presented in Fig. 1(d) with a strategy of 67° rotating scanning layer-by-layer. To achieve the appropriate apparent condition for subsequent characterization, the L-PBFed samples were mechanically ground and polished.

2.2 Microstructural characterization

Phase constituent was characterized by X-ray diffraction (XRD: Rigaku X−2000 diffractometer) with Cu K_α radiation. The spectra were recorded in the angle range of 20°−80° (2θ), and the scanning step was 0.1°. On the basis of the XRD pattern, the Williamson−Hall method [34] was used to calculate the dislocation density. L-PBFed samples were examined with the Archimedes method to determine their relative density. The apparent defects of L-PBFed samples were characterized by optical microscope (Leica DM4000M). The smaller-scale microstructural characteristics of the alloy samples were characterized by multiple electron microscope. Prior to SEM observation, L-PBFed samples were first etched using Keller reagent and

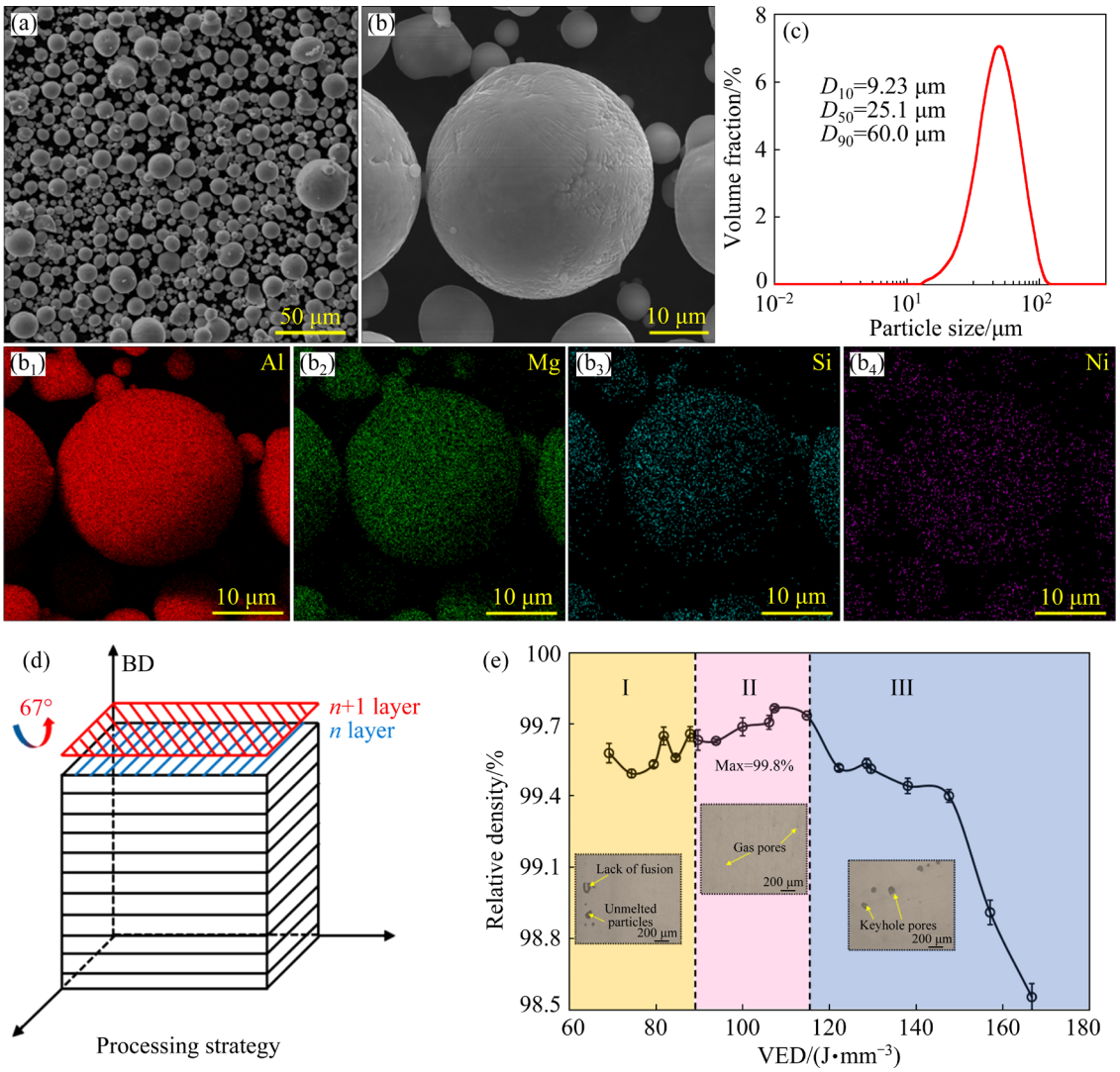

Fig. 1 SEM image of Al−5Mg_2Si−1.5Ni alloy powder (a), SEM−EDS mappings of single particle (b, b_1−b_4), particle size distribution of powders (c), diagram showing scanning strategy of L-PBF process (d), and relative density and optical micrographs (OM) of L-PBFed Al−5Mg_2Si−1.5Ni samples obtained at different volumetric energy densities (VEDs) (e)

then characterized using an FEI Nano230 field emission scanning electron microscope (FE-SEM). The crystallographic orientation and grain size of the L-PBFed samples were investigated by an FIB Helios Nanolab G3 UC system equipped with a Hikari camera and the TSL OIM data analysis software for electron backscattered diffraction (EBSD). Furthermore, the detailed microstructures were characterized by transmission electron microscope (TEM) with Tecnai G2 F20 operating at 200 kV. A combination of mechanical polishing and precision ion polishing system (PIPS) was used to prepare samples for TEM at a voltage of 2−5 kV and the incident angle of 3°−8°. Based on high angle annular dark field (HAADF) TEM images, the mean size and fraction of in-situ phases and fine grains can be estimated by ImageJ software.

2.3 Mechanical tests

The dog-bone tensile specimens (gauge length: 15 mm; width: 4 mm; depth: 2 mm) were machined by wire electrical discharge machining. Both sides of the sample were polished with 2000# silicon carbide sandpaper. The tensile testing at room temperature was conducted by MTS Alliance RT30 with the engineering strain rate of 1×10^{-3} s^{-1}. The tensile tests were carried out three times to ensure the repeatability.

3 Results

3.1 Densification behavior and processing formability

Generally, the relative density of L-PBF samples is significantly related to their formability. Figure 1(e) illustrates the relative density and representative defect features of L-PBFed Al−5Mg_2Si−1.5Ni alloy at different volumetric energy densities (VEDs). The VED can be normally expressed as follows [26]: VED=P/(vht), where P is the laser power (W), v is the scanning speed (mm/s), h is the hatch spacing (mm), and t is the layer thickness (mm). In Region I (in Fig. 1(e)) with the VED of 69.2−89 J/mm^3, the relative density increased slackly and the defects were mainly composed of the lack of fusion and un-melted particles. With the increase of the VED to Region II in Fig. 1(e) at 89−114.8 J/mm^3, the fluidity and wettability of liquid metal were significantly improved. The L-PBFed samples showed a peak relative density of 99.8% at the VED of 107.4 J/mm^3. Under this condition, only a small amount of gas pores could be observed. With further increasing the VED to Region III at 114.8−166.7 J/mm^3, the formation of keyhole pores was highly associated with the sharp decrease of the relative density.

3.2 Microstructural characteristics

3.2.1 Phase evolution during L-PBF

L-PBF process with extremely rapid melting and cooling process is normally associated with a non-equilibrium solidification condition. The CALPHAD method was developed for equilibrium solidification, but it is still valid for non-equilibrium solidification and therefore delivers a potential in facilitating the design of crack-free Al alloys [11,35,36]. The equilibrium phase diagrams of Al−$x$$Mg_2Si$ and Al−5Mg_2Si−xNi alloys calculated via the PanAl2022 thermodynamic database are presented in Figs. 2(a, c). It can be seen that the similarity among two types of alloys was that α-Al was preferentially formed as the primary matrix phase. However, there was an obvious difference in the subsequent eutectic solidification. In Al−5Mg_2Si alloys, the eutectic Mg_2Si phase was the only phase to be formed, but Mg_2Si and Al_3Ni phases were precipitated in the Al−5Mg_2Si−1.5Ni alloys. Figures 2(b, d) show the solidification paths of Al−5Mg_2Si and Al−5Mg_2Si−1.5Ni alloys calculated using the Gulliver−Scheil model. The precipitation sequences were: Liquid → α-Al → Mg_2Si, and Liquid → α-Al → Mg_2Si → Al_3Ni, respectively. For the Al−5Mg_2Si−1.5Ni alloy, Mg_2Si and Al_3Ni phases were formed when the temperature was lower than 852.3 and 849.8 K, respectively, indicating two eutectic reactions might exist in the alloy. The small solidification range (85.5 K) for primary solidification and eutectic solidification also offered a potential for micro-structural refinement.

In consistent with calculation results, XRD patterns of the pre-alloyed powder and L-PBFed Al−5Mg_2Si−1.5Ni alloy in Fig. 3(a) confirmed that the diffraction peaks of α-Al matrix and Mg_2Si phase could be obviously detected within the 2θ range of 20°−80° in both samples. And the weak diffraction peak intensity of Al_3Ni phase might be

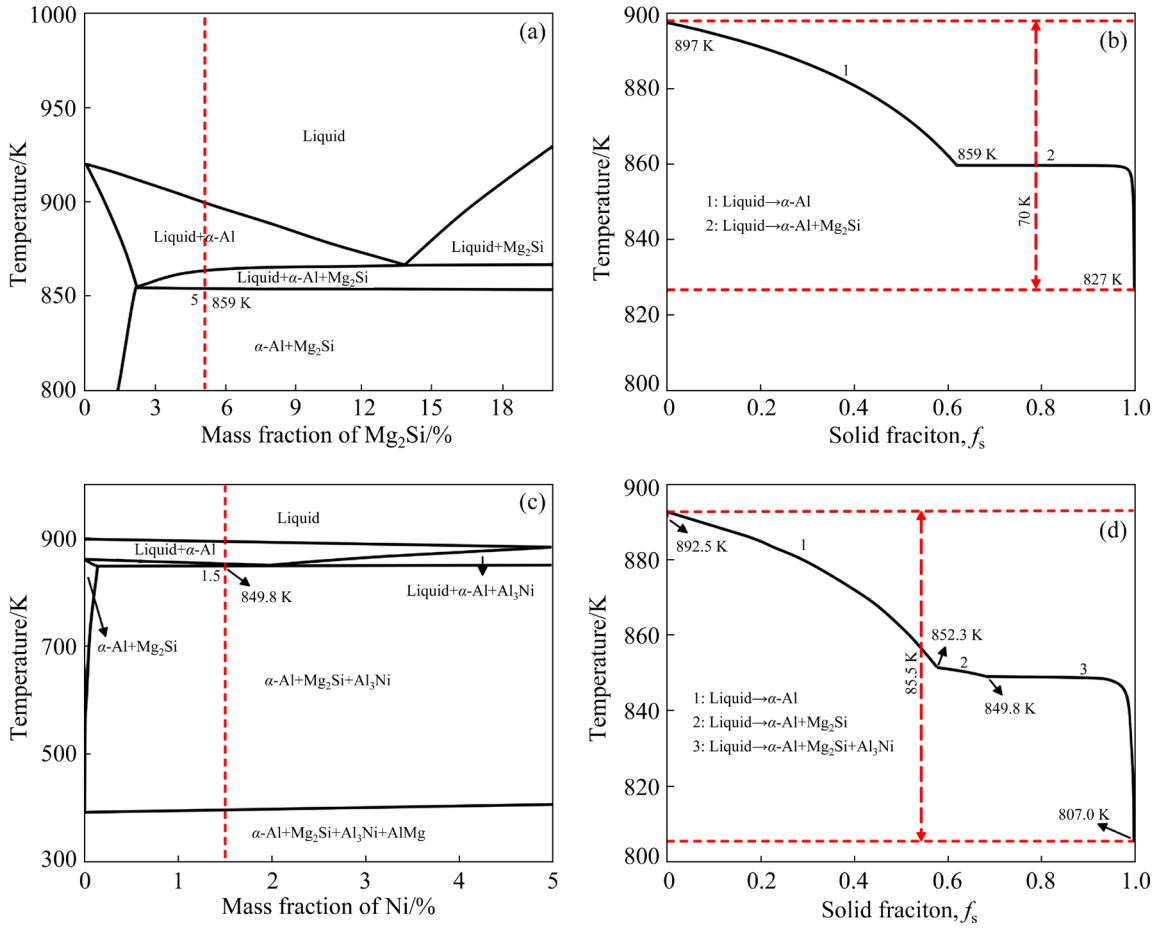

Fig. 2 Vertical sections of equilibrium phase diagrams for Al–xMg$_2$Si (a) and Al–5Mg$_2$Si–xNi (c) alloys, and solidification paths of Al–5Mg$_2$Si (b) and Al–5Mg$_2$Si–1.5Ni (d) alloys

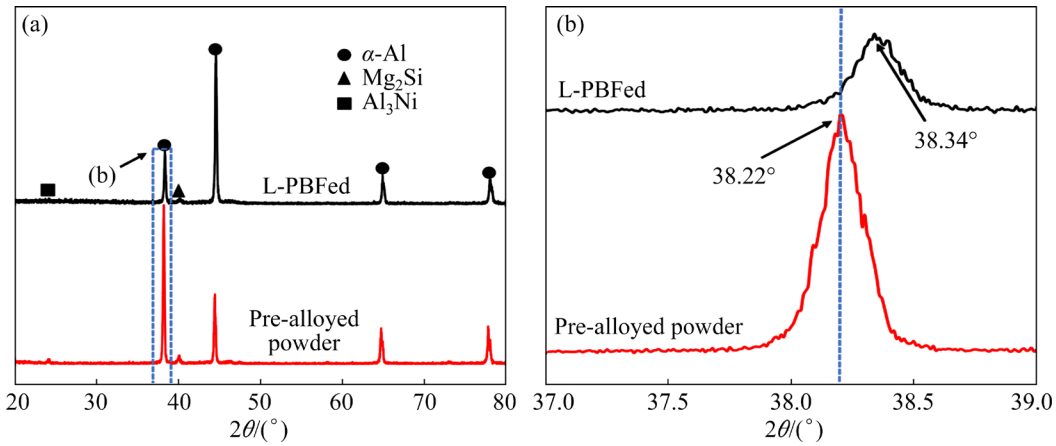

Fig. 3 XRD patterns for phase analysis in pre-alloyed powder and L-PBFed Al–5Mg$_2$Si–1.5Ni samples: (a) Overall spectra; (b) Detailed spectra at 2θ from 37.0° to 39.0°

associated with its low concentration and small scale of dimensions [6]. Furthermore, the diffraction peak of α-Al matrix slightly shifted to high angles after the L-PBF process, as indicated in Fig. 3(b). According to Bragg's equation, an increased angle leads to a smaller lattice constant. The large residual stress formed during the L-PBF process with sharp cooling rate promotes the crystal lattice distortion. And, the solid solution of elements in the α-Al matrix may also affect the crystal lattice

distortion further [6].

The growth restriction factor (Q) was calculated based on the solidification curves in Figs. 2(b, d), in which the solute addition (e.g., Ni) related to the increased constitutional undercooling (ΔT_{CS}) at the front of solid−liquid (S/L) interface normally results in the grain refinement [37−39]. Correspondingly, the ability of solute to produce ΔT_{CS} could be estimated by the calculation of Q value, which could be expressed as follows [40]:

$$Q=\left(\frac{\partial(\Delta T_{CS})}{\partial(f_s)}\right)_{f_s\to 0} \quad (1)$$

where the values of f_s and ΔT_{CS} can be acquired by Scheil−Gulliver simulation results. For the constrained Liquid→α-Al solidification, the calculation results of Q were 31.5 K in the Al−5Mg_2Si−1.5Ni alloy and 23.2 K in the Al−5Mg_2Si alloy. Although the Q value of Al−5Mg_2Si−1.5Ni alloy is not so high, the efficiency of Ni solutes for refining Al grains is higher than that of Si and Cu, which is similar to the previous work [41]. As such, the ability in grain refinement was strong in the Ni-contained alloy. On top of the solid solution of Ni solutes, the potential nucleation of Al_3Ni particles could also promote the grain refinement.

3.2.2 Formation of non-equilibrium microstructure

Calculation results suggested that a potential refined microstructure can be obtained in the Al−5Mg_2Si−1.5Ni alloy. And EBSD maps as well as SEM images in Fig. 4 further verified the formation of refined heterogeneous grains. The microstructures of the L-PBFed Al−5Mg_2Si−1.5Ni alloy along the building direction were featured by fine columnar grains with the size distribution ranging from 2 to 20 μm. The fine grains were formed around the melt pool boundaries due to the large temperature gradient and heat accumulation [42]. Compared to the L-PBFed Al−5Mg_2Si alloy, the addition of Ni decreased the size of α-Al grains from 24.4 to 14.6 μm (Figs. 4(a, b)). Meanwhile, SEM image in Fig. 4(c) confirmed that no obvious pores were observed from the low magnification image, which was consistent with the previously obtained high relative density (99.8%) (Fig. 1(e)). Furthermore, the typical hierarchical microstructure of L-PBFed Al−5Mg_2Si−1.5Ni alloy could be divided into heat-affected-zone (HAZ), coarse-grain-zone (CGZ) and fine-grain-zone (FGZ). The cellular structures that consist of α-Al matrix, and nanosized precipitates were distributed in all three regions (Fig. 4(d)). However, cellular structures distributed

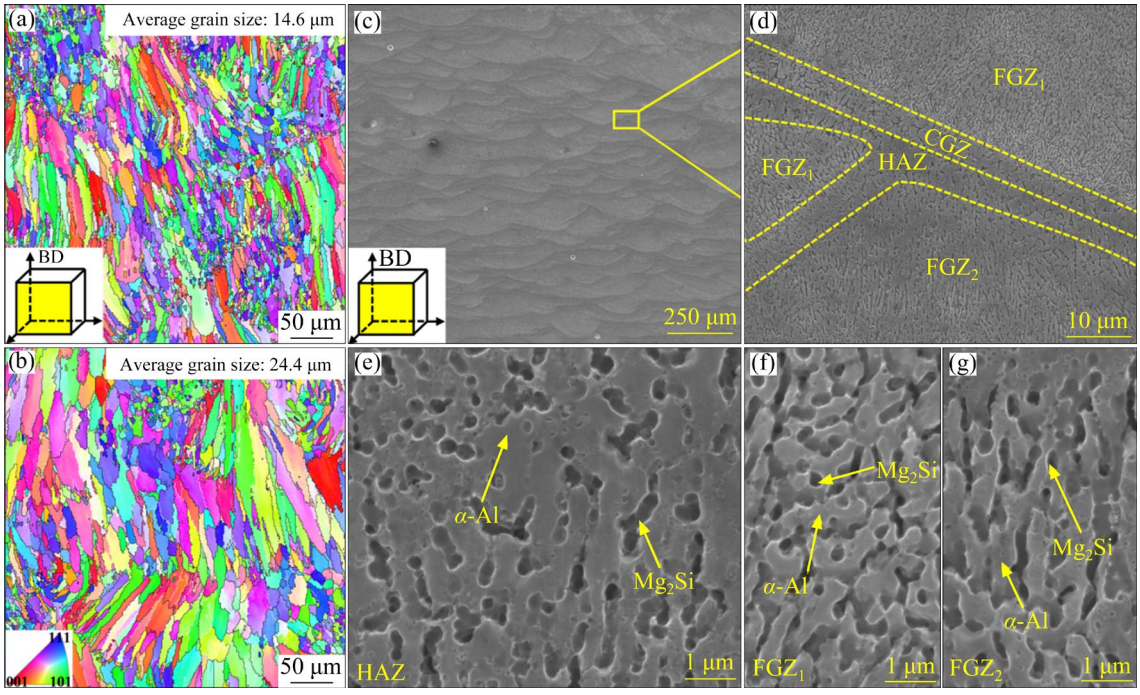

Fig. 4 IPF maps of L-PBFed Al−5Mg_2Si−1.5Ni (a) and Al−5Mg_2Si (b) alloys along building direction; (c−g) SEM micrographs of longitudinal section of L-PBFed Al−5Mg_2Si−1.5Ni alloy: (c) Low magnification image; (d) Overall microstructure; Detailed microstructures of HAZ (e), FGZ_1 (f) and FGZ_2 (g)

in the HAZ were partially broken up due to the continuous thermal cycling around the melting pool boundaries (Fig. 4(e)). Equiaxed cellular grains and columnar cellular grains were observed in FGZ_1 and FGZ_2, respectively. Furthermore, the dark-black separated Mg_2Si was individually distributed at the grain boundaries rather than as part of the cellular structures (Figs. 4(f, g)).

To characterize the detailed microstructures of the L-PBFed Al−5Mg_2Si−1.5Ni alloy systematically, TEM images including bright-field (BF) image, dark-field (DF) image, high-angle annular dark-field (HAADF) image and the corresponding EDS maps are shown in Fig. 5. The obvious hierarchical microstructures including FGZ, CGZ and HAZ could be observed in L-PBFed alloy, which was similar to SEM results (Fig. 4(d)). A considerable number of cellular structures decorated with (Al,Ni)-enriched and (Mg,Si)-enriched phases could be observed inside the α-Al matrix (Figs. 5(b, d, d_1−d_4)). The introduction of uniformly distributed (Al,Ni)-enriched and (Mg,Si)-enriched phases during L-PBF process were ascribed to the uniform elemental distribution in the pre-alloyed powder. The slight difference of morphology in HAZ was because (Al,Ni)- and (Mg,Si)-enriched phases had different degrees of coarsening. EDS results in Figs. 5(h_2, h_3) displayed the formation of

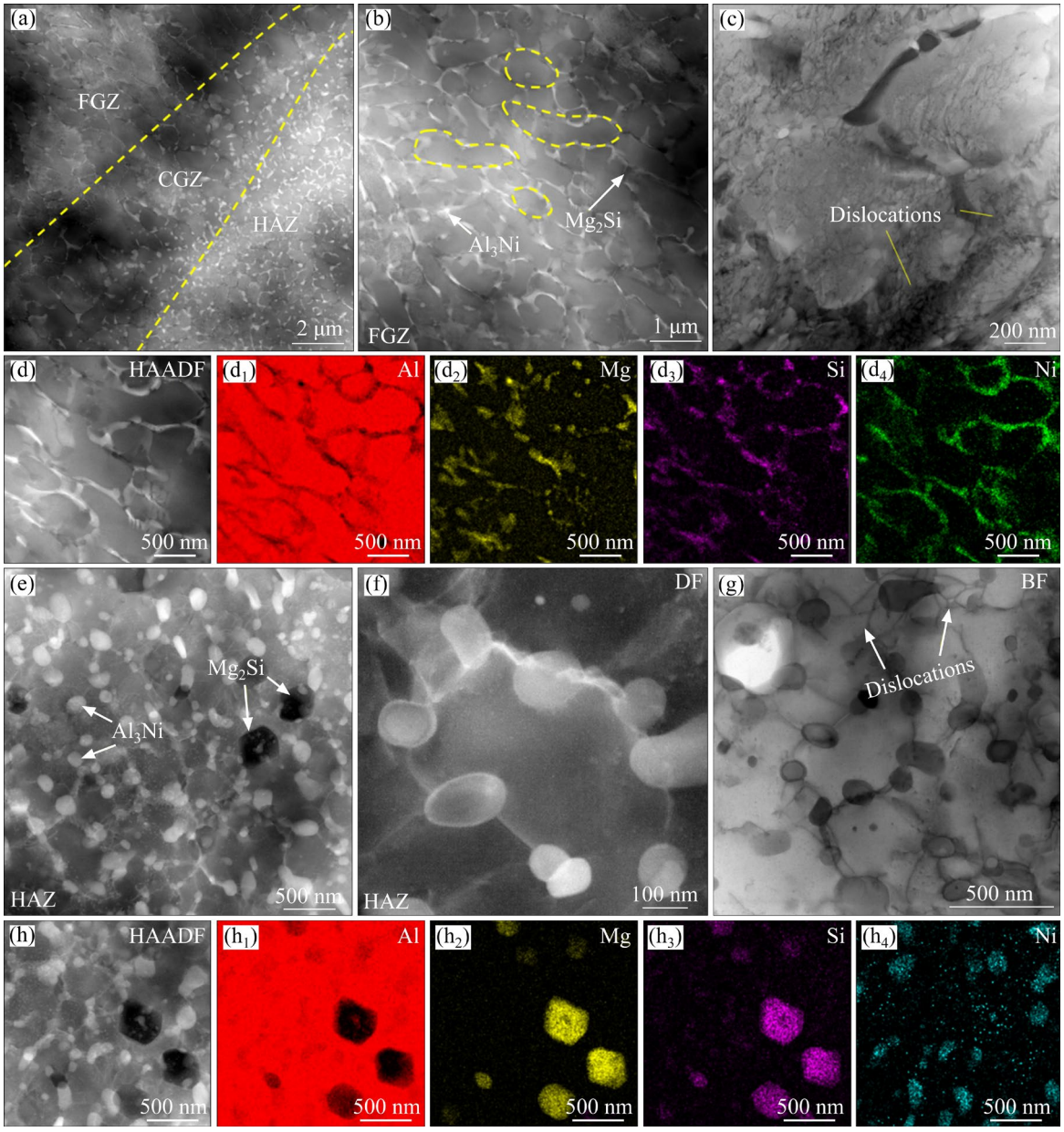

Fig. 5 TEM image of L-PBFed Al−5Mg_2Si−1.5Ni alloy (a); Detailed microstructure of FGZ and HAZ (b, e, f); TEM bright-field (BF) images showing distribution of dislocations (c, g); EDS maps of FGZ (d, d_1−d_4) and HAZ (h, h_1−h_4)

bulk (Mg,Si)-enriched phase with a size of 200−300 nm. Meanwhile, the (Al,Ni)-enriched phase distributed along the entire cellular structure boundaries could be detected in Figs. 5(e, h). A large number of dislocations entangled at the cellular boundaries could be also observed in Figs. 5(c, g).

Figures 6(a−f) show the high-resolution transmission electron microscope (HRTEM) images and Fast Fourier Transform (FFT) patterns of the interaction between α-Al matrix and two types of particles. Figures 6(a, d) and (b, e) confirmed that (Al,Ni)-enriched phases and bulk (Mg,Si)-enriched phases were Al_3Ni and Mg_2Si phases, respectively. It is different from the Al−5Mg_2Si alloy that no obvious Al−Mg_2Si eutectics were observed with the addition of Ni. The Al_3Ni nanoparticles located at the cellular structure boundaries and α-Al together constituted the Al−Al_3Ni cellular eutectics (Figs. 5(b, e)). This is because, following the precipitation of Mg_2Si, the main component of the remnant liquid phase was Al_3Ni, while the eutectic structures were the products of the eutectic reaction of the residual concentrated liquid at the cell boundaries during the terminal stage of solidification [43,44]. The orientation relationships between α-Al and Al_3Ni phase could be described as $(200)_{\alpha\text{-Al}}//(100)_{Al_3Ni}$, $(220)_{\alpha\text{-Al}}//(110)_{Al_3Ni}$ and $[001]_{\alpha\text{-Al}}//[001]_{Al_3Ni}$, which confirm that the Al_3Ni phase was semi-coherent with the α-Al. The Al_3Ni phase was coherent with the α-Al matrix along [001] matrix, with an interplanar spacing of 0.553 nm for the (001) plane of Al_3Ni phase (Fig. 6(c)). Also, the semi-coherent interface between α-Al and Mg_2Si could be expressed as $(11\bar{1})_{\alpha\text{-Al}}//(1\bar{1}1)_{Mg_2Si}$, $(1\bar{1}1)_{\alpha\text{-Al}}//(\bar{2}\bar{2}0)_{Mg_2Si}$ and $[011]_{\alpha\text{-Al}}//[1\bar{1}2]_{Mg_2Si}$, Mg_2Si phase was coherent with the α-Al matrix along [011] matrix, with an interplanar spacing of 0.389 nm for the $(1\bar{1}1)$ of the Mg_2Si phase (Fig. 6(f)). It is speculated that a good interface relationship between the nano-sized phases and the α-Al matrix results in Orowan strengthening among the Al alloys, and the interaction between nanoscale particles and dislocations promotes the formation of dislocation loops and improves the mechanical response significantly [26].

3.3 Mechanical properties

SEM and TEM analysis confirmed that a typical hierarchical microstructure was formed in the L-PBFed Al−5Mg_2Si−1.5Ni alloy. The refined

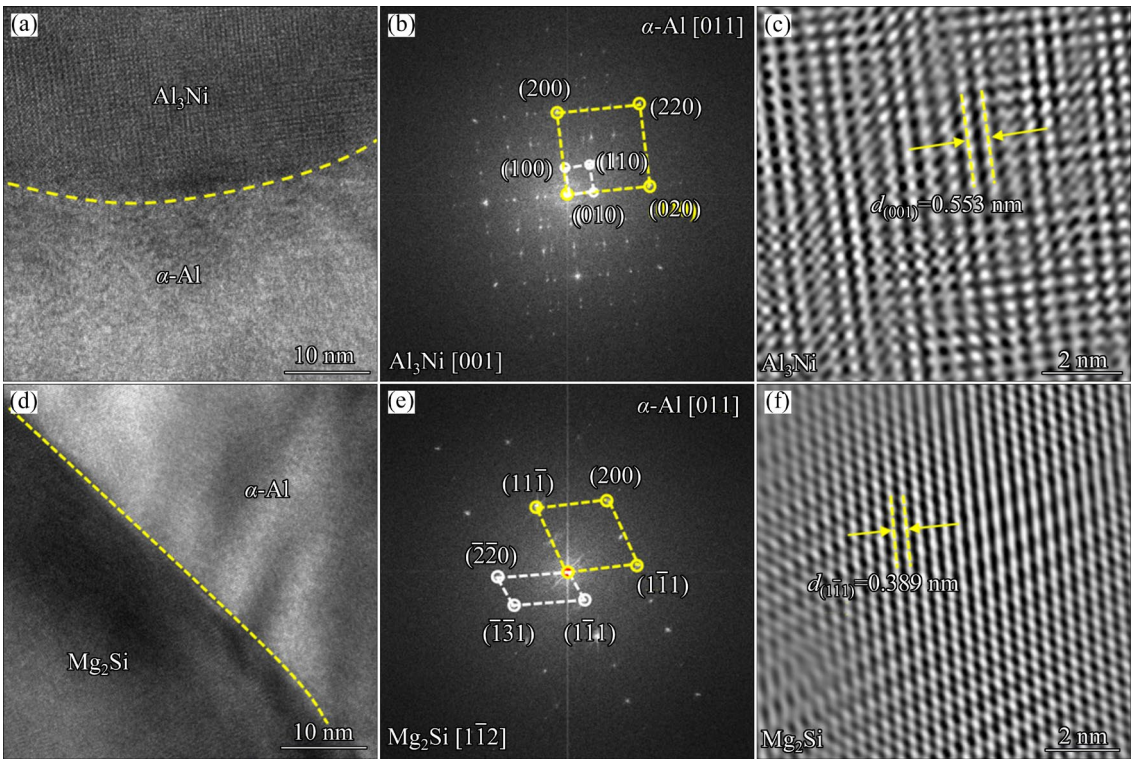

Fig. 6 HRTEM micrographs of interface between Al_3Ni phase and Al matrix (a), Mg_2Si phase and α-Al matrix (d), corresponding FFT patterns (b, e), and IFFT (Inverse Fast Fourier Transform) images (c, f)

heterogeneous α-Al matrix contained the interaction between the dislocations and the Al−Al_3Ni cellular eutectics as well as the Mg_2Si particles. These could deliver a huge potential in promoting strength enhancement. The tensile stress−strain curve of the L-PBFed Al−5Mg_2Si−1.5Ni alloy at the VED of 114.8 J/mm^3 showed a good combination of mechanical properties, in which the YS (yield strength) was (425±15) MPa, the UTS (ultimate tensile strength) was (541±11) MPa and the EL (elongation) was (6.2±0.2)% (Fig. 7(a)). It is indicated from Fig. 7(b) that the L-PBFed Al−5Mg_2Si−1.5Ni alloy represented a decent mechanical performance compared with other Al alloys manufactured by various techniques, including the L-PBFed Al−5Mg_2Si−2Mg [26] and Al− 5Mg_2Si−2Mg−2Fe [45], L-PBFed Al−Mg−Si [36,46,47], Al−Mg−Sc−Zr [48−50], Al−Mg−Si−Sc−Zr [51], Al−Zn−Mg−Cu [52,53], AlSi10Mg [54,55], AlSi12 [56], and as-cast Al−Mg−Si alloys [57−59]. Strikingly, the L-PBFed Al−5Mg_2Si−1.5Ni alloy exhibited higher strength response than L-PBFed AlSi10Mg, AlSi12 alloys and even the expensive Zr/Sc modified Al−Mg−Si alloys. Meanwhile, the fractured surface of the L-PBFed Al−5Mg_2Si−1.5Ni samples confirmed a typical combination of ductile−brittle fracture mode, in which substantial dimples and tearing ridges could be detected in Figs. 7(c−e) simultaneously. Such a feature of ductile−brittle mixed fracture was consistent with the moderate EL ((6.2±0.2)%) in the L-PBFed Al−5Mg_2Si−1.5Ni alloy.

4 Discussion

Based on the microstructural characteristics and our previous results in the L-PBFed Al−5Mg_2Si alloy [26], the Ni addition into Al−Mg_2Si alloy could result in the formation of Al−Al_3Ni cellular structures on top of the Al−Mg_2Si cellular structures. The advantages included: (1) the solid solubility limit of extra Mg atoms is more likely to be improved greatly via high cooling rate during L-PBF process; (2) similar to Al−Mg_2Si cellular structures, the introduction of Al−Al_3Ni cellular structures could offer a strong ability in eutectic filling and promote crack elimination (Fig. 1(e)); (3) combined with the increased Q value, the formation of Al_3Ni particles could play as nucleation sites to facilitate grain refinement; (4) although the

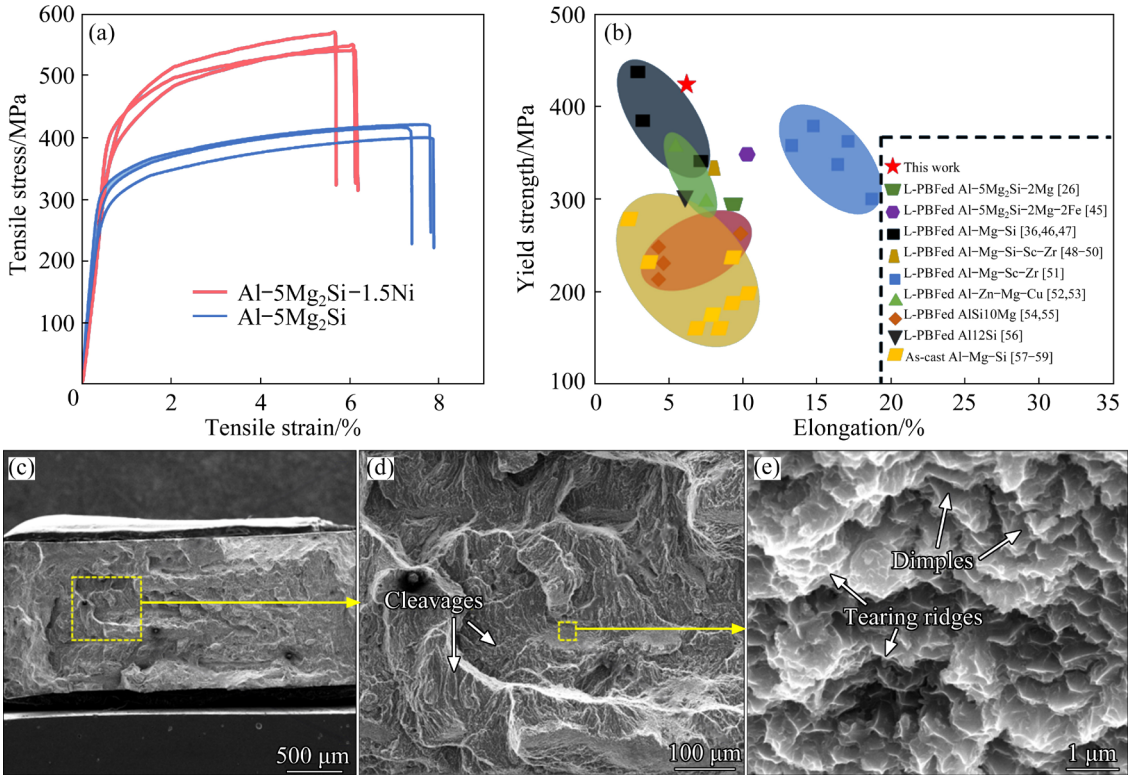

Fig. 7 Stress−strain curves (a), comparison of YS between L-PBFed Al−5Mg_2Si−1.5Ni alloy in this study and other L-PBFed [26,36,45−56] and as-cast [57−59] Al alloys (b), and SEM micrographs showing fractograph (c, d) and detailed dimples in fractured surface of sample at VED of 114.8 J/mm^3 (e)

precipitation strengthening effect of Mg_2Si is reduced (the preferential precipitation of Mg_2Si increases the size), the high density of fine Al_3Ni particles provides an effective strengthening effect; (5) an coherent orientation relationship between the Al_3Ni particles and the α-Al matrix could exert a positive influence on acquiring an excellent synergy of strength and ductility.

Considering that the mass ratio of Mg to Si in the Mg_2Si phase is 1.73, the element content in Table 1 implies that excessive Mg (~1.47 wt.%) is dissolved in the α-Al matrix, which is higher than that of Mg solution (0.6 wt.%) in conventional casting/wrought methods [60]. Moreover, the solid solution strengthening of Ni is not embraced in this work owing to the low solid solubility of Ni in α-Al matrix [61]. The potential solid solution strengthening (σ_{SS}) of the alloy can, thus, be expressed as [62]

$$\sigma_{SS}=k_j c_j^{2/3} \tag{2}$$

where j represents Mg, c_j is the concentration of Mg in solid solution (wt.%) and k_j is the corresponding scaling factor: k_{Mg}=29.0 MPa/wt.%$^{2/3}$ [62]. Thus, the YS improvement related to solid solution strengthening is calculated to be 37.5 MPa.

Besides the solid solution of Mg solutes associated with the increased constitutional undercooling (ΔT_{CS}) and the Q value, the nucleation of Al_3Ni particles in eutectics could also promote the grain refinement. According to the Hall−Petch equation [30], the contribution of grain boundary strengthening (σ_{gb}) to YS can be described as

$$\sigma_{gb}=k_y d^{-1/2} \tag{3}$$

where k_y is a constant of 0.04 MPa·m$^{1/2}$ [30] and d is the average grain size (14.6 μm). The estimated contribution of grain boundary strengthening is 10.5 MPa.

Correspondingly, the illustration diagram of microstructural characteristics is shown in Fig. 8. It is also noted that the formation of melting cracks and cellular structures in Figs. 8(a, b) was dominated by the production of temperature gradient (ΔT) and cooling rate (R), and the refined structures could be obtained via the high value of the $\Delta T \cdot R$. It is noteworthy that the specific large temperature gradient and heat accumulation induce a unique cellular structure arrangement. According to the solidification path, Mg_2Si was preferentially formed, and Al_3Ni was then precipitated at the final stage of solidification to form Al_3Ni particles within α-Al matrix. In this stage, the remnant liquid phase trapped at the cellular structure boundaries was likely participated by eutectic reaction and finally formed a typical Al−Al_3Ni cellular structure (Fig. 8(c)). Thus, the design of crack-free Al−5Mg_2Si−1.5Ni alloy with narrow solidification range and high Q value offers a potential in achieving the superior combination of strength and ductility.

Moreover, a high number density of dislocations generally occur in the alloy samples due to the high cooling rate in L-PBF process. The dislocations tangling with each other improve the mechanical properties significantly. BF-TEM images in Figs. 5(c, g) also indicated that the interaction between the high number density of dislocations and the Al_3Ni as well as the trace of Mg_2Si phase builds a solid foundation for dislocation strengthening and precipitation strengthening. The concerning

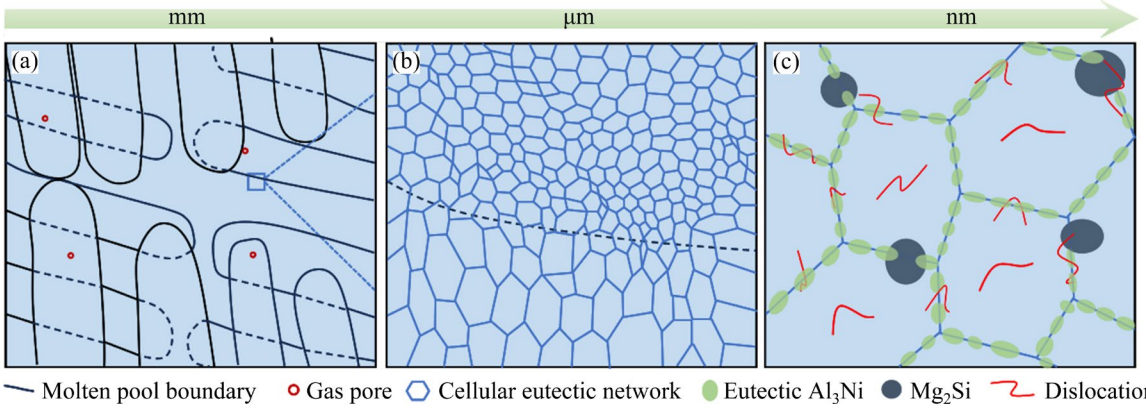

Fig. 8 Schematic illustration showing microstructural characteristics of L-PBFed Al−5Mg_2Si−1.5Ni alloy on different scales: (a) Millimeter; (b) Micrometer; (c) Nanometer

contribution can be expressed by the Bailey−Hirsch formula [29]:

$$\sigma_{dis}=M\alpha Gb\rho^{1/2} \quad (4)$$

where M is Taylor factor of 3.06, α is a constant of 0.24 for FCC metals, G is the shear modulus of the α-Al matrix (26 GPa), b is the amplitude of Burger vector of 0.286 nm for α-Al matrix, and ρ is the dislocation density. The dislocation density was roughly estimated by the Williamson−Hall method [34] based on the XRD pattern. XRD diffraction peak broadening (β) includes two parts, the crystallite size broadening (β_G) and the strain broadening (β_S). Based on the hypothesis of Cauchy-type function, these can be described as [29]

$$\beta=\beta_G+\beta_S \quad (5)$$

$$\beta_G=K\lambda/(D\cdot\cos\theta) \quad (6)$$

$$\beta_S=4\varepsilon\cdot\tan\theta \quad (7)$$

where K is a constant of 0.9, λ(=0.15405 nm) is the wavelength of Cu K_α radiation, D is the crystallite size, θ is the Bragg angle of the certain peak and ε is the microstrain. Equation (5) can be also expressed as

$$\beta\cdot\cos\theta=K\lambda/D+(4\sin\theta)\varepsilon \quad (8)$$

According to Eq. (8), the parameter ε is the gradient of the linear regression of the $\beta\cos\theta$−$4\sin\theta$ plot (Calculated to be 0.0016). Then, the dislocation density can be calculated by the subsequent formula:

$$\rho=2\sqrt{3}\varepsilon/(Db) \quad (9)$$

where the dislocation density is 7.20×10^{14} m^{-2}, and the estimated strength increment to YS by dislocation strengthening is 147 MPa.

Finally, nano-sized Al_3Ni and Mg_2Si particles are detected. Especially, good interface matching relationship exists between the precipitated particles and α-Al matrix (Fig. 6). The precipitated particles can hinder the movement of dislocations and results in Orowan strengthening. The contribution to yield strength by precipitate strengthening (σ_{pt}) can be expressed as [63]

$$\sigma_{pt}=\frac{0.4MGb}{\pi(1-\nu)^{1/2}}\frac{\ln(2\bar{r}/b)}{\lambda_1} \quad (10)$$

where M is Taylor factor of 3.1; ν is the Poisson's ratio (0.33); $\bar{r}$ is the mean radius of spherical precipitates on a circular cross section in a random plane, $\bar{r}=\sqrt{2/3}r$, where r is the mean radius of the precipitates; λ_1 is the interval spacing between nano-particles in the glide plane, which is linked with $\bar{r}$ and the volume fraction f_v of the nano-particles, and can be described as follows [64]:

$$\lambda_1=2\bar{r}\left(\sqrt{\frac{\pi}{4f_v}}-1\right) \quad (11)$$

Based on SEM and TEM images, the precipitate strengthening for Al_3Ni with a mean radius of 48.2 nm and volume fraction of 2.16% can be calculated to be 50.9 MPa. The precipitate strengthening for Mg_2Si with a mean radius of 58.9 nm and volume fraction of 5.8% can be calculated to be 80.9 MPa. The introduction of Al−Al_3Ni eutectics with Ni addition promotes an effective precipitation strengthening. The yield strength of the pure aluminium (σ_0, ~60 MPa [65,66]) should be also taken into account. Additionally, the comparison of calculated yield strength and experimental yield strength is shown in Fig. 9. The calculated theoretical value is close to the experimental results. It can be found that the main contributions to the yield strength of the designed L-PBFed Al−5Mg_2Si−1.5Ni alloy are precipitation strengthening and dislocation strengthening.

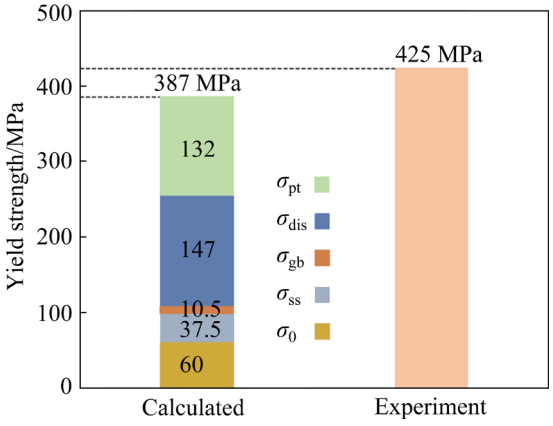

Fig. 9 Comparison of calculated and experimental YS

In summary, the introduction of Ni (1.5 wt.%) into the L-PBFed Al−5Mg_2Si alloy induces the significantly improvement in the ability of grain refinement and strength enhancement. Among there, the formation of bulk Mg_2Si particles during the initial stage of solidification and the introduction of the eutectics that constitute the α-Al matrix and Al_3Ni particles located at the cellular structure boundaries during the final stage of solidification,

are mainly responsible for the generation of a refined hierarchical structure with a high relative density of 99.8%. Meanwhile, the interaction between a high quantity density of dislocations and nano-sized Al_3Ni as well as Mg_2Si particles in the L-PBFed Al−5Mg_2Si−1.5Ni alloy delivers an excellent synergy of strength−ductility, in which UTS and EL reach up to (541±11) MPa and (6.2±0.2)%, respectively.

5 Conclusions

(1) The formation of fine equiaxed structure with Al−Al_3Ni eutectics could be obtained in the L-PBFed crack-free Ni-modified Al−5Mg_2Si samples with a high relative density of 99.8% at the VED of 107.4 J/mm^3. The increased constitutional supercooling and the growth restriction factor induced via Ni addition resulted in the formation of a fine grain structure (14.6 μm).

(2) The L-PBFed Al−5Mg_2Si−1.5Ni alloy offered superior mechanical properties with the YS of (425±15) MPa, the UTS of (541±11) MPa and the EL of (6.2±0.2)%. Strengthening mainly initiated from the refined heterogeneous α-Al matrix grains that contained Al−Al_3Ni eutectics and Mg_2Si particles, which acted as strong barriers to dislocation motion. Ni addition delivered a superior synergic effect of grain refinement, dislocation strengthening and precipitation strengthening.

(3) The introduction of Al−Al_3Ni eutectics with Ni addition offered a creative design method for the high-strength Al−Mg−Si alloy capable of additive manufacturing process.

CRediT authorship contribution statement

Yi-mou LUO: Data curation, Writing − Original draft, Investigation; **Jian-ying WANG** and **Tao WEN:** Investigation, Writing − Review & editing; **Fei-peng YANG**, **Meng-zhen ZHU**, **Na HE**, **Jian-ming ZHENG**, and **Ling SHAN:** Investigation; **Hai-lin YANG:** Conceptualization, Funding acquisition, Project administration, Writing − Review & editing, Supervision.

Declaration of competing interest

The authors declare that they have no known competing financial interests or personal relationships that could have appeared to influence the work reported in this paper.

Acknowledgements

Financial supports from the National Natural Science Foundation of China (No. 52071343) and the Leading Innovation and Entrepreneurship Team of Zhejiang Province, China — Automotive Light Alloy Innovation Team (No. 2022R01018) are gratefully acknowledged.

References

[1] WAWRZYNIAK N, PROVENCHER P R, BROCHU M, BROCHU M. Tensile properties of SS316L produced by LPBF: Influence of specimen dimensions and surface condition [J]. Materials Characterization, 2023, 203: 113117.

[2] YANG Fei-peng, WEN Tao, ZHANG Lei, WANG Jian-ying, HUANG Shi-long, JI Shou-xun, YANG Hai-lin. Role of inclination angle on columnar-to-equiaxed transition in the eutectic Al−5Mg−2Si alloy fabricated by laser powder bed fusion [J]. Journal of Central South University, 2024, 31: 2150−2166.

[3] HAN Chang-jun, FANG Qi-hong, SHI Yu-sheng, TOR S B, CHUA C K, ZHOU Kun. Recent advances on high-entropy alloys for 3D printing [J]. Advanced Materials, 2020, 32: e1903855.

[4] WANG Jian-ying, YANG Hai-lin, LIU Zhi-lin, FAN Lei, YAN Wen-tao, QIU Dong, FU Ming-wang. Compositional regulation in additive manufacturing of precipitation-hardening $(CoCrNi)_{94}Ti_3Al_3$ medium-entropy superalloy: Cellular structure stabilization and strength enhancement [J]. Composites (Part B): Engineering, 2024, 281: 111570.

[5] WANG Jin-cheng, ZHU Rui, LIU Yu-jing, ZHANG Lai-chang. Understanding melt pool characteristics in laser powder bed fusion: An overview of single- and multi-track melt pools for process optimization [J]. Advanced Powder Materials, 2023, 2: 100137.

[6] YANG Fei-peng, WANG Jian-ying, WEN Tao, ZHANG Lei, DONG Xi-xi, QIU Dong, YANG Hai-lin, JI Shou-xun. Developing a novel high-strength Al−Mg−Zn−Si alloy for laser powder bed fusion [J]. Materials Science and Engineering A, 2022, 851: 143636.

[7] KOTADIA H R, GIBBONS G, DAS A, HOWES P D. A review of laser powder bed fusion additive manufacturing of aluminum alloys: Microstructure and properties [J]. Additive Manufacturing, 2021, 46: 102155.

[8] ZHU Zhi-guang, FERN L N, HANG L S, LU Wen-jun, CHRISTIAN H L, RAO Zi-yuan, DIERK R, SHARON M L N. Superior mechanical properties of a selective-laser-melted AlZnMgCuScZr alloy enabled by a tunable hierarchical microstructure and dual-nanoprecipitation [J]. Materials Today, 2022, 52: 90−101.

[9] LI Gan, ZHAO Chun-lu, HUANG Yu-he, TAN Qi-yang, HOU Jun-hua, HE Xi, GUO Chuan, LU Wen-jun, ZHOU Lin, LIU Si-da, ZHANG Lei, CHEN Xu-liang, LI Xing-gang, LI Ying, LUAN Jun-hua, LI Zhen-min, MAO Xin-ping, ZHANG Ming-xing, ZHU Qiang, LU Jian. Additively manufactured fine-grained ultrahigh-strength bulk aluminum alloys with nanostructured strengthening defects [J].

Materials Today, 2024, 76: 40−51.

[10] JI Yuan-yuan, XU Yun-ze, ZHANG Bin-bin, BEHNAMIAN Y, XIA Da-hai, HU Wen-bin. Review of micro-scale and atomic-scale corrosion mechanisms of second phases in aluminum alloys [J]. Transactions of Nonferrous Metals Society of China, 2021, 31: 3205−3227.

[11] ZHANG Jin-liang, GAO Jian-bao, SONG Bo, ZHANG Li-jun, HAN Chang-jun, CAI Chao, ZHOU Kun, SHI Yu-sheng. A novel crack-free Ti-modified Al−Cu−Mg alloy designed for selective laser melting [J]. Additive Manufacturing, 2021, 38: 101829.

[12] ABOULKHAIR N T, SIMONELLI M, PARRY L, ASHCROFT I, TUCK C, HAGUE R. 3D printing of aluminum alloys: Additive manufacturing of aluminum alloys using selective laser melting [J]. Progress in Materials Science, 2019, 106: 100578.

[13] LAI Yi, DENG Ying, ZHU Xin-wen, GUO Yi-fan, XU Guo-fu, HUANG Ji-wu, YIN Zhi-min. Tensile property and microstructure of Al−4.77Mn−1.37Mg−0.67Sc−0.25Zr alloy under different selective laser melting processing parameters [J]. Transactions of Nonferrous Metals Society of China, 2023, 33: 357−370.

[14] ZHANG Jin-liang, SONG Bo, WEI Qing-song, BOURELL D, SHI Yu-sheng. A review of selective laser melting of aluminum alloys: Processing, microstructure, property and developing trends [J]. Journal of Materials Science & Technology, 2019, 35: 270−284.

[15] ROMETSCH P A, ZHU Yu-man, WU Xin-hua, HUANG Ai-jun. Review of high-strength aluminium alloys for additive manufacturing by laser powder bed fusion [J]. Materials & Design, 2022, 219: 110779.

[16] MEHTA A, ZHOU Le, HUYNH T, PARK S, HYER H, SONG Shu-tao, BAI Yuan-li, IMHOLTE N N, WOOLSTENHULME N E, WACHS D M, SOHN Y. Additive manufacturing and mechanical properties of the dense and crack free Zr-modified aluminum alloy 6061 fabricated by the laser-powder bed fusion [J]. Additive Manufacturing, 2021, 41: 101966.

[17] STOPYRA W, GRUBER K, SMOLINA I, KURZYNOWSKI T, KUŹNICKA B. Laser powder bed fusion of AA7075 alloy: Influence of process parameters on porosity and hot cracking [J]. Additive Manufacturing, 2020, 35: 101270.

[18] BOSIO F, SHEN Hao-peng, LIU Yang, LOMBARDI M, ROMETSCH P, WU Xin-hua, ZHU Yu-man, HUANG Ai-jun. Production strategy for manufacturing large-scale AlSi10Mg components by laser powder bed fusion [J]. JOM, 2021, 73: 770−780.

[19] HE Zhu-bin, LIANG Jiang-kai, ZHANG Hai-ming, GUO En-yu, DU Wei, POLITIS D J, WANG Li-liang. Formability and microstructure of laser powder bed fused AlSi10Mg alloy sheets under various deformation conditions [J]. Materials Characterization, 2023, 199: 112813.

[20] READ N, WANG Wei, ESSA K, ATTALLAH M M. Selective laser melting of AlSi10Mg alloy: Process optimization and mechanical properties development [J]. Materials & Design, 2015, 65: 417−424.

[21] WANG Wei, ZHANG Yu-bo, YUE Cong-cong, KONG Xiang-qing, HAO Zhi-gang, WANG Tong-min, LI Ting-ju. Processing defect, microstructure evolution and mechanical properties of laser powder bed fusion Al−12Si alloys [J]. Journal of Materials Research and Technology, 2023, 26: 681−696.

[22] GAIN A K, ZHANG Liang-chi. Tribological behavior of eutectic Al−12Si alloy manufactured by selective laser melting [J]. Wear, 2023, 522: 204679.

[23] WANG Yue-ting, LI Rui-di, YUAN Tie-chui, ZOU Liang, WANG Min-bo, YANG Hai-ou. Microstructure and mechanical properties of Al−Fe−Sc−Zr alloy additively manufactured by selective laser melting [J]. Materials Characterization, 2021, 180: 111397.

[24] LV Hai-yang, PENG Peng, FENG Ting, GAO Hai-yan, JU Jiang, WANG Bing, WANG Jun, SUN Bao-de. High-performance co-continuous Al−Ce−Mg alloy with in-situ nano-network structure fabricated by laser powder bed fusion [J]. Additive Manufacturing, 2022, 60: 103218.

[25] RÖDLER G, FISCHER F G, PREUßNER J, FRIEDMANN V, FISCHER C, WEISHEIT A, SCHLEIFENBAUM J H. Additive manufacturing of high-strength eutectic aluminium-nickel alloys—Processing and mechanical properties [J]. Journal of Materials Processing Technology, 2021, 298: 117315.

[26] YANG Hai-lin, ZHANG Ying-ying, WANG Jian-ying, LIU Zhi-lin, LIU Chun-hui, JI Shou-xun. Additive manufacturing of a high strength Al−5Mg_2Si−2Mg alloy: Microstructure and mechanical properties [J]. Journal of Materials Science & Technology, 2021, 91: 215−223.

[27] WANG Jian-ying, YANG Fei-peng, YANG Hai-lin, ZHANG Li-jun, ZHANG Ying-ying, LIU Zhi-lin, JI Shou-xun. Effect of heat treatment on the microstructure and mechanical properties of an Al−5Mg_2Si−2Mg alloy processed by laser powder bed fusion [J]. Journal of Alloys and Compounds, 2022, 920: 165944.

[28] WEN Tao, WANG Jian-ying, LI Zhi-cheng, YANG Fei-peng, LIU Zhi-lin, YANG Hai-lin, JI Shou-xun. Microstructural evolution and strengthening mechanisms of a high-strength Al−Mg−Si alloy processed by laser powder bed fusion and ageing treatment [J]. Materials Characterization, 2024, 209: 113754.

[29] WEN Tao, LI Zhi-cheng, WANG Jian-ying, LUO Yi-mou, YANG Fei-peng, LIU Zhi-lin, QIU Dong, YANG Hai-lin, JI Shou-xun. From crack-prone to crack-free: Eliminating cracks in additively manufacturing of high-strength Mg_2Si-modified Al−Mg−Si alloys [J]. Journal of Materials Science & Technology, 2025, 204: 276−291.

[30] HANSEN N. Hall−Petch relation and boundary strengthening [J]. Scripta Materialia, 2004, 51: 801−806.

[31] SUWANPREECHA C, PANDEE P, PATAKHAM U, LIMMANEEVICHITR C. New generation of eutectic Al−Ni casting alloys for elevated temperature services [J]. Materials Science and Engineering A, 2018, 709: 46−54.

[32] DENG Jun-wang, CHEN Chao, LIU Xiao-chun, LI Yun-ping, ZHOU Ke-chao, GUO Sheng-min. A high-strength heat-resistant Al−5.7Ni eutectic alloy with spherical Al_3Ni nano-particles by selective laser melting [J]. Scripta Materialia, 2021, 203: 114034.

[33] DEILLON L, JENSCH F, PALM F, BAMBACH M. A new

high strength Al−Mg−Sc alloy for laser powder bed fusion with calcium addition to effectively prevent magnesium evaporation [J]. Journal of Materials Processing Technology, 2022, 300: 117416.

[34] HE J Y, WANG H, HUANG H L, XU X D, CHEN M W, WU Y, LIU X J, NIEH T G, AN K, LU Z P. A precipitation-hardened high-entropy alloy with outstanding tensile properties [J]. Acta Materialia, 2016, 102: 187−196.

[35] WANG Q Z, KANG N, LIN X, MANSORI M E, HUANG W D. High strength Al−Cu−Mg based alloy with synchronous improved tensile properties and hot-cracking resistance suitable for laser powder bed fusion [J]. Journal of Materials Science & Technology, 2023, 141: 155−170.

[36] LI Feng, LI Zhi-cheng, TANG Cheng-lu, ZHANG Li-jun, TAN Qi-yang, CHEN Chao, ZHANG Ming-xing, ZHOU Ke-chao. Design high-strength Al−Mg−Si alloy fabricated by laser powder bed fusion: Cracking suppression and strengthening mechanism [J]. Materials Science and Engineering A, 2023, 864: 144591.

[37] RYEN Ø, HOLMEDAL B, NIJS O, NES E, SJÖLANDER E, EKSTRÖM H E. Strengthening mechanisms in solid solution aluminum alloys [J]. Metallurgical and Materials Transactions A, 2006, 37: 1999−2006.

[38] AZARNIYA A, TAHERI A K, TAHERI K K. Recent advances in ageing of 7xxx series aluminum alloys: A physical metallurgy perspective [J]. Journal of Alloys and Compounds, 2019, 781: 945−983.

[39] LI Gan, HUANG Yu-he, LI Xin-wei, GUO Chuan, ZHU Qiang, LU Jian. Laser powder bed fusion of nano-titania modified 2219 aluminium alloy with superior mechanical properties at both room and elevated temperatures: The significant impact of solute [J]. Additive Manufacturing, 2022, 60: 103296.

[40] QUESTED T E, DINSDALE A T, GREER A L. Thermodynamic modelling of growth−restriction effects in aluminium alloys [J]. Acta Materialia, 2005, 53: 1323−1334.

[41] TAN Qi-yang, YIN Yu, PRASAD A, LI Gan, ZHU Qiang, STJOHN D H, ZHANG Ming-xing. Demonstrating the roles of solute and nucleant in grain refinement of additively manufactured aluminium alloys [J]. Additive Manufacturing, 2022, 49: 102516.

[42] WANG Zi-hong, ZENG Ling-guo, LIN Xin, WANG Jing-feng, FENG Zhe, DANG Cong, LI Hong-yun, WANG Yan-fang, HUANG Wei-dong. Microstructural evolution and strengthening mechanisms of additively-manufactured Al−Mg−Sc−Zr alloys: Laser directed energy deposition versus laser powder bed fusion [J]. Journal of Alloys and Compounds, 2024, 985: 173946.

[43] WU J, WANG X Q, WANG W, ATTALLAH M M, LORETTO M H. Microstructure and strength of selectively laser melted $AlSi_{10}Mg$ [J]. Acta Materialia, 2016, 117: 311−320.

[44] PRASHANTH K G, ECKERT J. Formation of metastable cellular microstructures in selective laser melted alloys [J]. Journal of Alloys and Compounds, 2017, 707: 27−34.

[45] WANG Jian-ying, GAO Jian-bao, YANG Hai-lin, YANG Fei-peng, WEN Tao, LIU Zhi-lin, ZHANG Li-jun, JI Shou-xun. High-strength Al−5Mg−2Si−2Mg−2Fe alloy with extremely high Fe content for green industrial application through additive manufacturing [J]. Virtual and Physical Prototyping, 2023, 18: e2235587.

[46] YANG Fei-peng, WANG Jian-ying, WEN Tao, AI Xin-hai, DONG Xi-xi, YANG Hai-lin, JI Shou-xun. Microstructure and mechanical properties of pseudo binary eutectic Al−Mg_2Si alloy processed by laser powder bed fusion [J]. Journal of Materials Research and Technology, 2023, 24: 2187−2199.

[47] GENG Yao-xiang, WANG Qing, WANG Ying-min, ZANG Qian-hao, MI Shao-bo, XU Jun-hua, XIAO Ya-kai, WU Yi, LUAN Jun-hua. Microstructural evolution and strengthening mechanism of high-strength $AlSi_{8.1}Mg_{1.4}$ alloy produced by selective laser melting [J]. Materials & Design, 2022, 218: 110674.

[48] EKUBARU Y, GOKCEKAYA O, ISHIMOTO T, SATO K, MANABE K, WANG P, NAKANO T. Excellent strength−ductility balance of Sc−Zr-modified Al−Mg alloy by tuning bimodal microstructure via hatch spacing in laser powder bed fusion [J]. Materials & Design, 2022, 221: 110976.

[49] LI Xiang, LIU Yun-zhong, TAN Chao-lin, ZOU Yong-ming. Laser powder bed fusion of a novel crack-free Al−Mg−Sc−Zr alloy: Printability, microstructure characterization and mechanical performance [J]. Optics & Laser Technology, 2023, 162: 109281.

[50] LI Xiang, LIU Yun-zhong. Microstructure characterization and mechanical performance of laser powder bed fusion processed AlMgScZr alloy: Effect of heat treatment [J]. Materials Science and Engineering A, 2023, 862: 144501.

[51] BI Jiang, LEI Zheng-long, CHEN Yan-bin, CHEN Xi, TIAN Ze, LIANG Jing-wei, QIN Xi-kun, ZHANG Xin-rui. Densification, microstructure and mechanical properties of an Al−14.1Mg−0.47Si−0.31Sc−0.17Zr alloy printed by selective laser melting [J]. Materials Science and Engineering A, 2020, 774: 138931.

[52] LIU Xiao-hui, LIU Yun-zhong, ZHOU Zhi-guang, ZHAN Qiang-kun. Enhanced strength and ductility in Al−Zn−Mg−Cu alloys fabricated by laser powder bed fusion using a synergistic grain-refining strategy [J]. Journal of Materials Science & Technology, 2022, 124: 41−52.

[53] LI Lan-bo, YUAN Tie-chui, FENG Bo. The microstructures and mechanical properties of Al−Zn−Mg−Cu−Si−Zr alloy: A comparison between directed energy deposition and laser powder bed fusion [J]. Materials Letters, 2023, 337: 133959.

[54] PARK T H, BAEK M S, HYER H, SOHN Y, LEE K A. Effect of direct aging on the microstructure and tensile properties of AlSi10Mg alloy manufactured by selective laser melting process [J]. Materials Characterization, 2021, 176: 111113.

[55] PATAKHAM U, PALASAY A, WILA P, TONGSRI R. MPB characteristics and Si morphologies on mechanical properties and fracture behavior of SLM AlSi10Mg [J]. Materials Science and Engineering A, 2021, 821: 141602.

[56] AI Xin-hai, WANG Jian-ying, WEN Tao, YANG Fei-peng, DONG Xi-xi, YANG Hai-lin, JI Shou-xun. A high Fe-containing AlSi12 alloy fabricated by laser powder bed fusion [J]. Journal of Materials Research and Technology, 2022, 18: 4513−4521.

[57] CAI Qing, MENDIS C L, CHANG I T H, FAN Zhong-yun.

Microstructure evolution and mechanical properties of new die-cast Al−Si−Mg−Mn alloys [J]. Materials & Design, 2020, 187: 108394.
[58] WEI Bo, PAN Shuai, LIAO Gui-zhen, ALI A, WANG Shuang-bao. Sc-containing hierarchical phase structures to improve the mechanical and corrosion resistant properties of Al−Mg−Si alloy [J]. Materials & Design, 2022, 218: 110699.
[59] PRACH O, TRUDONOSHYN O, RANDELZHOFER P, KÖRNER C, DURST K. Effect of Zr, Cr and Sc on the Al−Mg−Si−Mn high-pressure die casting alloys [J]. Materials Science and Engineering A, 2019, 759: 603−612.
[60] SJÖLANDER E, SEIFEDDINE S. The heat treatment of Al−Si−Cu−Mg casting alloys [J]. Journal of Materials Processing Technology, 2010, 210: 1249−1259.
[61] DING Han, XIAO Ya-kai, BIAN Ze-yu, WU Yi, YANG Hui-hui, WANG Hong-ze, WANG Hao-wei. Design, microstructure and thermal stability of a novel heat-resistant Al−Fe−Ni alloy manufactured by selective laser melting [J]. Journal of Alloys and Compounds, 2021, 885: 160949.
[62] MYHR O R, GRONG Ø, ANDERSEN S J. Modelling of the age hardening behaviour of Al−Mg−Si alloys [J]. Acta Materialia, 2001, 49: 65−75.
[63] MA Ka-ka, WEN Hai-ming, HU Tao, TOPPING T D, ISHEIM D, SEIDMAN D N, LAVERNIA E J, SCHOENUNG J M. Mechanical behavior and strengthening mechanisms in ultrafine-grain precipitation-strengthened aluminum alloy [J]. Acta Materialia, 2014, 62: 141−155.
[64] HU Zhi-heng, ZHANG Hu, ZHU Hai-hong, XIAO Zhong-xu, NIE Xiao-jia, ZENG Xiao-yan. Microstructure, mechanical properties and strengthening mechanisms of $AlCu_5MnCdVA$ aluminum alloy fabricated by selective laser melting [J]. Materials Science and Engineering A, 2019, 759: 154−166.
[65] VO N Q, DUNAND D C, SEIDMAN D N. Atom probe tomographic study of a friction-stir-processed Al−Mg−Sc alloy [J]. Acta Materialia, 2012, 60: 7078−7089.
[66] LI Rui-di, WANG Min-bo, LI Zhi-ming, CAO Peng, YUAN Tie-chui, ZHU Hong-bin. Developing a high-strength Al−Mg−Si−Sc−Zr alloy for selective laser melting: Crack-inhibiting and multiple strengthening mechanisms [J]. Acta Materialia, 2020, 193: 83−98.

Ni 对激光粉末床熔融 Al−Mg−Si 合金显微组织及力学性能的影响

罗懿谋[1]，汪建英[1]，文 涛[1]，杨飞鹏[1]，朱梦真[1]，何 娜[1]，郑建明[2]，单 玲[2]，杨海林[1]

1. 中南大学 粉末冶金国家重点实验室，长沙 410083；
2. 浙江万丰精密铸造有限公司，绍兴 312400

摘 要：对激光粉末床熔融(L-PBF)制备的高强 Al−5Mg_2Si−1.5Ni 合金的显微组织及力学性能进行系统研究。结果表明，在 Al−5Mg_2Si 合金中引入 1.5%(质量分数)的 Ni 可以显著改善 L-PBF 成形性能并提升力学性能。当体积能量密度为 107.4 J/mm^3 时，Ni 改性 Al−5Mg_2Si 合金的凝固区间仅为 85.5 K，并且获得了典型的 Al−Al_3Ni 共晶组织，合金相对密度达到 99.8%。此外，细化的分层组织主要表现为平均尺寸为 14.6 μm 的非均匀 α-Al 晶粒以及位错与 Al−Al_3Ni 共晶和 Mg_2Si 间的交互作用。在 Ni 添加引起的晶粒细化、位错强化和析出强化协同作用下，L-PBF 成形 Al−5Mg_2Si−1.5Ni 合金获得了优异的力学性能，其屈服强度为(425±15) MPa，极限抗拉强度为(541±11) MPa，伸长率为(6.2±0.2)%。

关键词：激光粉末床熔融；Al−Mg−Si 合金；显微组织演变；力学性能；强化机制

(Edited by Wei-ping CHEN)